The Astrophysical Journal, 897:171 (9pp), 2020 July 10 https://doi.org/10.3847/1538-4357/ab9649

A White Dwarf with Transiting Circumstellar Material Far outside the Roche Limit

Z. Vanderbosch[1,2], J. J. Hermes[3], E. Dennihy[4], B. H. Dunlap[1], P. Izquierdo[5,6], P.-E. Tremblay[7], P. B. Cho[1,2], B. T. Gänsicke[7], O. Toloza[7], K. J. Bell[8,9], M. H. Montgomery[1,2], and D. E. Winget[1,2]
[1] Department of Astronomy, University of Texas at Austin, Austin, TX 78712, USA; zvanderbosch@astro.as.utexas.edu
[2] McDonald Observatory, Fort Davis, TX 79734, USA
[3] Department of Astronomy, Boston University, Boston, MA 02215, USA
[4] Gemini Observatory, Casilla 603, La Serena, Chile
[5] Instituto de Astrofísica de Canarias, E-38205 La Laguna, Tenerife, Spain
[6] Departamento de Astrofísica, Universidad de La Laguna, E-38206 La Laguna, Tenerife, Spain
[7] Department of Physics, University of Warwick, Coventry CV4 7AL, UK
[8] DIRAC Institute, Department of Astronomy, University of Washington, Seattle, WA 98195, USA
Received 2019 August 22; revised 2020 May 21; accepted 2020 May 23; published 2020 July 15

Abstract

We report the discovery of a white dwarf exhibiting deep, irregularly shaped transits, indicative of circumstellar planetary debris. Using Zwicky Transient Facility DR2 photometry of ZTF J013906.17+524536.89 and follow-up observations from the Las Cumbres Observatory, we identify multiple transit events that recur every ≈107.2 days, much longer than the 4.5–4.9 hr orbital periods observed in WD 1145+017, the only other white dwarf known with transiting planetary debris. The transits vary in both depth and duration, lasting 15–25 days and reaching 20%–45% dips in flux. Optical spectra reveal strong Balmer lines, identifying the white dwarf as a DA with $T_{\rm eff} = 10,530 \pm 140$ K and $\log(g) = 7.86 \pm 0.06$. A Ca II K absorption feature is present in all spectra both in and out of transit. Spectra obtained during one night at roughly 15% transit depth show increased Ca II K absorption with a model atmospheric fit suggesting [Ca/H] $= -4.6 \pm 0.3$, whereas spectra taken on three nights out of transit have [Ca/H] of −5.5, −5.3, and −4.9 with similar uncertainties. While the Ca II K line strength varies by only 2σ, we consider a predominantly interstellar origin for Ca absorption unlikely. We suggest a larger column density of circumstellar metallic gas along the line of site or increased accretion of material onto the white dwarf's surface are responsible for the Ca absorption, but further spectroscopic studies are required. In addition, high-speed time series photometry out of transit reveals variability with periods of 900 and 1030 s, consistent with ZZ Ceti pulsations.

Unified Astronomy Thesaurus concepts: White dwarf stars (1799); Transits (1711); Eclipses (442); Debris disks (363); Planetesimals (1259); Circumstellar dust (236); Stellar pulsations (1625); Tidal disruption (1696); Roche limit (1404); Circumstellar gas (238)

1. Introduction

The vast majority of currently known planet hosts will one day become white dwarfs, the end products of stellar evolution for low- to intermediate-mass stars ($M < 10\,M_{\odot}$, Williams et al. 2009). Many planets are expected to survive the post-main-sequence evolution of their host stars (Veras 2016). Indeed, at least one-third of all known white dwarfs with $T_{\rm eff} < 20{,}000$ K exhibit heavy elements beyond hydrogen and helium in their photospheres (Zuckerman et al. 2010; Koester et al. 2014), which is commonly interpreted as the active accretion of tidally disrupted planetary debris (Debes & Sigurdsson 2002; Jura 2003; Zuckerman et al. 2010; Veras et al. 2014; Farihi 2016; Mustill et al. 2018).

This debris has been detected in more than 40 white dwarfs as an infrared excess indicative of circumstellar dust, while in a small number of these systems, a gaseous debris component is detected via Ca II triplet emission (Farihi 2016). Only one white dwarf, however, exhibits transits caused by planetary material, WD 1145+017 (Vanderburg et al. 2015), which displays both photometric and spectroscopic signatures of transiting debris in 4.5–4.9 hr orbits.

In this manuscript, we report the discovery of a second white dwarf, ZTF J013906.17+524536.89 (hereafter ZTF J0139+5245), exhibiting photometric and spectroscopic evidence for transits caused by circumstellar planetary debris. In the following sections, we present publicly archived and newly obtained photometry and spectroscopy that constrain the white dwarf and its circumstellar material.

2. Observations

2.1. Public ZTF Photometry

We discovered two transits in ZTF J0139+5245 during a general search for variable white dwarfs in the public Zwicky Transient Facility (ZTF) survey (Masci et al. 2019; Bellm et al. 2019) by cross-matching the Gaia DR2 catalog of white dwarfs (Gentile Fusillo et al. 2019, hereafter GF19) with the public ZTF transient alert database (Patterson et al. 2019) using the API provided by the Las Cumbres Observatory Make Alerts Really Simple (MARS) project.[10] Prior to the cross-match, we trimmed the full GF19 catalog into an astrometrically clean, 200 pc sample of ≈40,000 objects using the criteria recommended by Lindegren et al. (2018) and Evans et al. (2018). As of 2019 May 8, this cross-match results in 783 objects that have at least one alert from ZTF indicative of transient or periodically variable behavior. We downloaded the public ZTF DR2 light curves for each object with an alert and visually

[9] NSF Astronomy and Astrophysics Postdoctoral Fellow.

[10] https://Mars.lco.global/

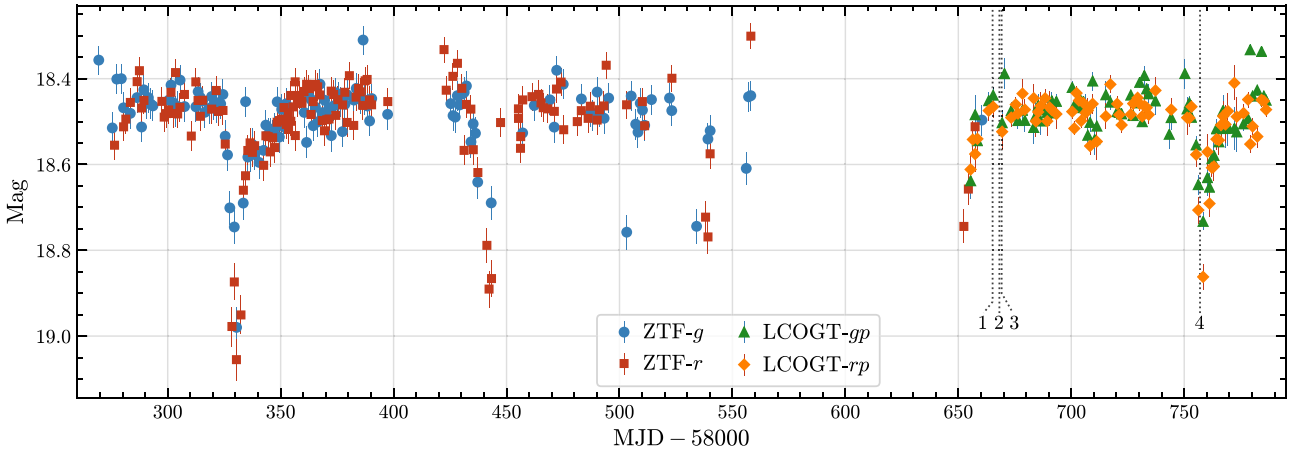

Figure 1. Light curve for ZTF J0139+5245 from ZTF DR2 and LCOGT observations. Three full transits are observed along with a partial transit at the start of LCOGT monitoring (MJD $\simeq$ 58650). While sparsely observed, an additional transit event may be seen near MJD $\simeq$ 58540. Magnitudes in the ZTF-*g* and *r* bands are shown with blue circles and red squares, respectively, while magnitudes in the LCOGT-*gp* and *rp* bands are shown with green triangles and orange squares, respectively. The average MJD for each of the four nights of WHT/ISIS spectroscopic observations is labeled with a vertical dotted line.

inspected them and their periodograms for signs of variability. ZTF J0139+5245 stood out as the only object with long-lasting, well-defined dips in flux (see Figure 1).

In total, ZTF J0139+5245 was covered by 279 public ZTF observations deemed of good photometric quality by the ZTF pipeline. We filtered these observations by only selecting points where *catflags* = 0, a condition for generating clean light curves recommended in the ZTF Science Data System Explanatory Supplement.[11] The final light curve for ZTF J0139+5245, shown in Figure 1, has 266 data points (128 in *g* and 138 in *r*) with a median temporal separation between observations of 22.4 hr with occasional large, multiday gaps. ZTF photometry is on the AB magnitude scale, calibrated using Pan-STARRS1 Survey (PS1) sources (Masci et al. 2019).

2.2. LCOGT Photometry

We began monitoring ZTF J0139+5245 on 2019 June 21 using the Las Cumbres Observatory Global Telescope (LCOGT) 1.0 m telescope network and have since observed the third full transit along with a partial transit event (see Figure 1).

We requested one to six observations each night with exposures between two and three minutes long in both *gp* and *rp* filters using the Sinistro imaging instrument (Brown et al. 2013). Completed observations were bias, dark, and flat-field corrected via the BANZAI pipeline.[12] We performed circular aperture photometry on all sources detected within each image using the `Photutils` package in Python (Bradley et al. 2019) and then cross-matched them with known PS1 sources. We measured the difference between PS1 and instrumental magnitudes ($m_d = m_{\rm PS1} - m_{\rm LCOGT}$) while filtering for outliers and likely galaxy candidates. We converted our instrumental magnitudes to apparent magnitudes on the PS1 scale by solving for a zero-point offset (z) and color term (c) with a least-squares fit to $m_d = z + c(g_{\rm PS1} - r_{\rm PS1})$.

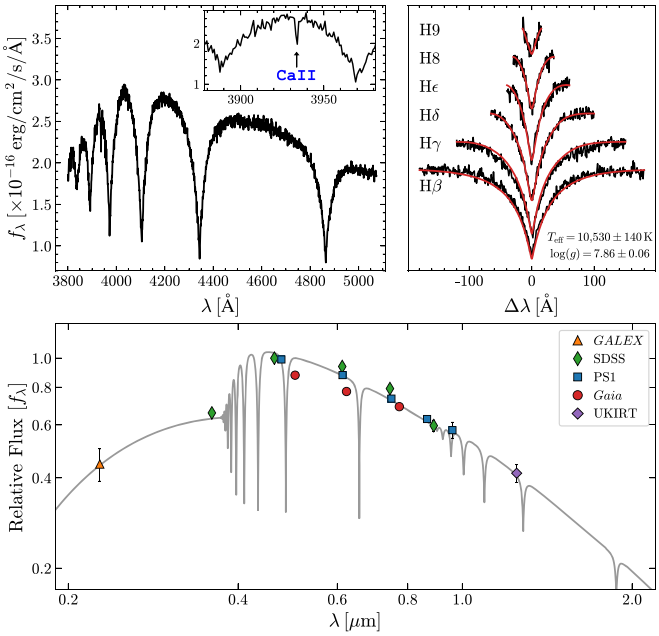

Figure 2. WHT/ISIS optical spectrum and SED of ZTF J0139+5245. The top left panel shows the combined spectrum for the first three nights of observations, taken out-of-transit, with an inset plot highlighting the Ca II K absorption feature at 3934Å. The top right panel shows the fit to the six Balmer lines, Hβ – H9, from which we derive spectroscopic log(g) and $T_{\rm eff}$ values (see Section 3.1). The bottom panel shows the SED with photometric data dereddened using the reddening law of Fitzpatrick (1999) and Indebetouw et al. (2005) with $E(B-V) = 0.12$ and $A_V = 0.38$. We overplot a model spectrum (gray line, Koester 2010) with $T_{\rm eff} = 10,500$ K and log(g) = 7.75 representing a good match to the shape of the observed SED.

2.3. WHT/ISIS Spectroscopy

We carried out spectroscopic observations of ZTF J0139+5245 on 2019 June 30, July 3, July 4, and September 30 using the Intermediate-dispersion Spectrograph and Imaging System (ISIS), mounted on the 4.2 m William Herschel Telescope (WHT) in La Palma, Spain (see Figures 2 and 3). The first three nights occurred outside of any deep transit event, but did occur just a few days after the nearest transit. Limits on transit depth for these three nights are <5%. The fourth night

[11] http://web.ipac.caltech.edu/staff/fmasci/ztf/ztf_pipelines_deliverables.pdf
[12] https://github.com/LCOGT/banzai

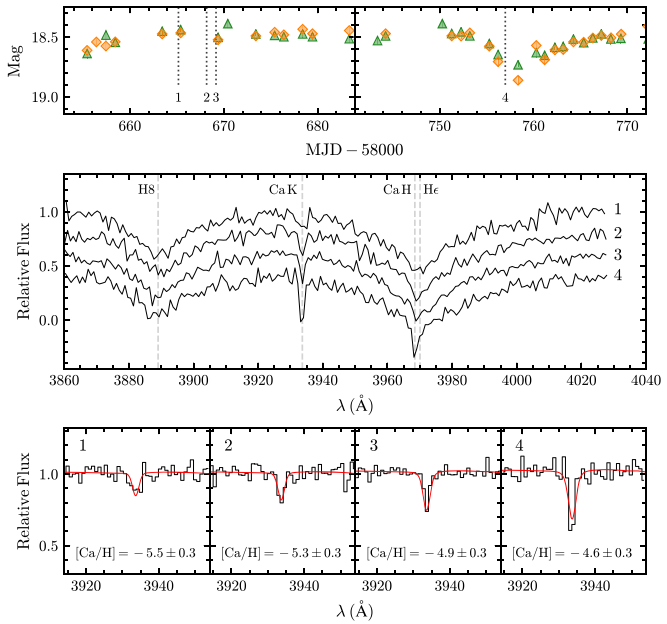

Figure 3. WHT/ISIS spectra in normalized flux units for each night, focused on the Ca II H and K absorption features. The top panels show zoomed in portions of the LCOGT *gp* (blue circles) and *rp* (red squares) photometry with the average MJD for each night's combined spectrum labeled with a vertical dotted line. The middle panel shows a broader wavelength region with spectra vertically stacked for comparison, while the bottom panels display model fits (red line) to the Ca II K line assuming a purely photospheric origin for Ca. The derived [Ca/H] photospheric abundance is given for each night, but we caution that the observed Ca absorption may also result from an increase in the column density of circumstellar metallic gas along the line of sight, in which case these [Ca/H] values are overestimates of the photospheric abundance (see Section 3.2).

occurred during a transit event at roughly 15% transit depth (see labels 1–4 in Figures 1 and 3).

We performed the observations using a 1″ slit and 600 line mm^{-1} grating in the blue (3800–5200 Å) arm of the spectrograph, achieving 1.9 Å resolution. Each night we took a series of consecutive 20 minute exposures under clear sky conditions with seeing values of 0.″6–1.″0 and an average airmass of 1.5. We obtained a total of 17 exposures on nights one through three, and six exposures on night four, for combined exposure times of 5.7 hr and 2.0 hr, respectively.

We applied bias, flat-field, and cosmic-ray corrections to our spectra using standard procedures within IRAF. We optimally extracted the one-dimensional spectrum (Horne 1986) using the data reduction software PAMELA. We used MOLLY (Marsh 1989) to wavelength and flux-calibrate the spectra by fitting a fourth-order polynomial to the HgArNeXe arc data and a five-knot spline to the spectrophotometric standard star, respectively. Arcs and standards were obtained using the same instrument setup just before and after the science observations were carried out.

2.4. Additional Survey Data

We compiled all available photometric and astrometric data for ZTF J0139+5245 from the Galaxy Evolution Explorer (GALEX; Martin et al. 2005; Morrissey et al. 2005), Gaia DR2 (Gaia Collaboration et al. 2018), the Sloan Digital Sky Survey (SDSS) DR9 (Ahn et al. 2012), the Pan-STARRS1 Survey (Chambers et al. 2016) DR2, and the United Kingdom Infra-Red Telescope (UKIRT) Hemisphere Survey (UHS, Dye et al. 2018). The compiled data are summarized in Table 1 while the spectral energy distribution (SED) is displayed in Figure 2.

Table 1
ZTF J0139+5245 Summary of Properties

α, δ (J2000)	$01^h\ 39^m06\overset{s}{.}17$, $+52°45'36\overset{''}{.}89$[1]	
μ_α, μ_δ (mas yr^{-1})	87.32 ± 0.39, 4.99 ± 0.43[1]	
ϖ (mas)	5.77 ± 0.25[1]	
d (pc)	172.9 ± 7.4[1]	
$T_{\rm eff}^{\rm 3D}$ (K)	$10,530 \pm 140$[2]	
$\log(g)^{\rm 3D}$ (cgs)	7.86 ± 0.06[2]	
M_* ($M_\odot$)	0.52 ± 0.03[2]	
NUV	19.89 ± 0.14[3,4]	
G	18.594 ± 0.008[1]	
$G_{\rm BP}$	18.55 ± 0.02[1]	
$G_{\rm RP}$	18.64 ± 0.03[1]	
	SDSS[5]	PS1[6]
u	19.04 ± 0.04	
g	18.46 ± 0.01	18.48 ± 0.01
r	18.40 ± 0.01	18.49 ± 0.01
i	18.52 ± 0.01	18.59 ± 0.01
z	18.75 ± 0.04	18.69 ± 0.02
y		18.78 ± 0.03
J	19.10 ± 0.07[7]	

Note. All magnitudes are on the AB scale. Gaia and UKIRT were converted from Vega to AB scales using the Gaia DR2 documentation (https://gea.esac.esa.int/archive/documentation/GDR2/) and Hewett et al. (2006), respectively.

References. (1) Gaia Collaboration et al. (2018), (2) this work, (3) Martin et al. (2005), (4) Morrissey et al. (2005), (5) Ahn et al. (2012), (6) Chambers et al. (2016), (7) Dye et al. (2018).

The PS1 3π survey (Kaiser et al. 2010; Magnier et al. 2013) is multiepoch, so we also obtained all individual detections to look for additional transit events. In total, ZTF J0139+5245 was observed by PS1 63 times over the course of 4.4 yr. To filter out poor-quality detections, we first removed those where >5% of the fitted PSF model was contaminated by bad pixels. To further filter our data, we followed the methods of Fulton et al. (2014). The resulting PS1 data contain 52 epochal detections (g:11, r:9, i:11, z:10, y:11) with 30–80 s exposure times.

2.5. McDonald 2.1 m Photometry

We acquired high-speed time-series photometry on four nights between 2019 June 26 and July 1 and on five nights between 2019 August 27 and September 3 using the Princeton Instruments ProEM frame-transfer CCD attached to the McDonald Observatory 2.1 m Otto Struve telescope (see Figure 4). We used Astrodon Gen2 Sloan g' and r' filters in an automated filter wheel with 15 to 30 s exposure times. Target availability limited our June–July runs to ∼1 hr each night, while our August–September runs ranged between 2.6 and 5.3 hr, for a total of 23.1 hr. We used IRAF to bias, dark, and flat-field correct the McDonald data using standard calibration frames taken before each night of observations. We performed circular aperture photometry using the IRAF routine CCD_HSP (Kanaan et al. 2002). Lastly, we used the WQED software suite to generate light curves with the optimal aperture size and apply a barycentric correction to the midexposure timestamp of each image (Thompson & Mullally 2013).

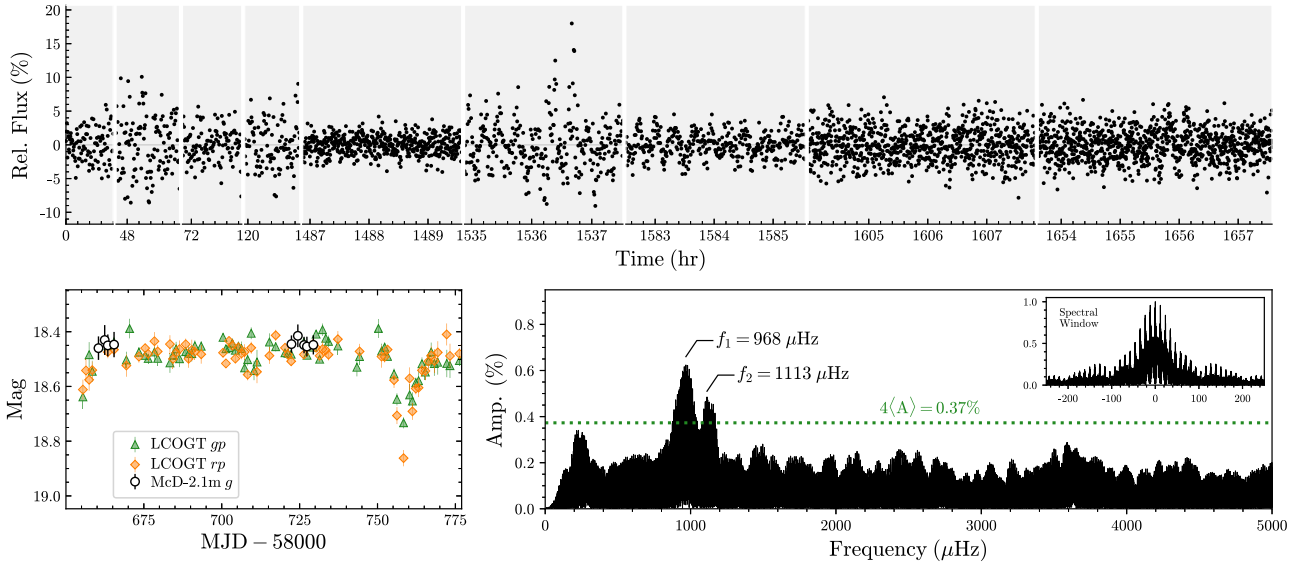

Figure 4. Nine nights of McDonald 2.1 m high-speed photometry taken out of transit show variability indicative of ZZ Ceti pulsations. The top panel shows the *g*- and *r*-band photometry for each night, normalized relative to six comparison stars within the field of view. The bottom left panel shows the average brightness for each night of McDonald *g*-band data relative to LCOGT observations, indicating the observations were taken out of transit. The Lomb–Scargle periodogram of the combined light curve is shown in the bottom right panel with two significant peaks labeled by their frequencies. The periodogram's $4\langle A \rangle$ significance threshold is denoted by the green dotted line.

3. Results

3.1. White Dwarf Atmospheric Parameters

Prior to obtaining a spectrum, ZTF J0139+5245 was considered a high probability white dwarf candidate due to both its SDSS photometric colors (Girven et al. 2011) and its location in the Gaia color–magnitude diagram (GF19). Utilizing Gaia photometry and parallax, GF19 report $T_{\rm eff} = 9{,}420 \pm 580$ K, $\log(g) = 7.87 \pm 0.21$, and $M_* = 0.52 \pm 0.11\ M_\odot$ for ZTF J0139+5245 assuming a pure-H atmosphere.

The newly obtained spectra provide clear evidence that ZTF J0139+5245 is a white dwarf of spectral type DA due to the presence of broad H-Balmer absorption features (see Figure 2). Using the combined spectrum for the three nights of observations taken out-of-transit, we fit six Balmer lines, Hβ − H9, utilizing the one-dimensional (1D) models and fitting procedures described in Tremblay et al. (2011). We find $T_{\rm eff}^{\rm 1D} = 10,790 \pm 140$ K and $\log(g)^{\rm 1D} = 8.09 \pm 0.06$ whose formal uncertainties have been added in quadrature to 1.2% $T_{\rm eff}$ and 0.038 dex $\log(g)$ uncertainties to account for typical systematics (Liebert et al. 2005). We apply corrections to these 1D values based on the three-dimensional (3D) convection simulations of Tremblay et al. (2013) to obtain $T_{\rm eff}^{\rm 3D} = 10,530 \pm 140$ K and $\log(g)^{\rm 3D} = 7.86 \pm 0.06$. Utilizing the 3D values and the white dwarf evolutionary models of Fontaine et al. (2001) with evenly mixed C/O cores and thick-H layers, we obtain $M_* = 0.52 \pm 0.03\ M_\odot$.

Using the best-fit spectroscopic temperature, we find a good match between a single white dwarf model SED (Koester 2010) and the observed SED with extinction and reddening corrections applied to the observed SED of $A_V = 0.38$ and $E(B-V) = 0.12$ (see Figure 2). The distance scaling relation of GF19 estimates less extinction for ZTF J0139+5245 with $A_V = 0.11$, as does the 3D reddening map of Capitanio et al. (2017) with $A_V = 0.16 \pm 0.06$. The full Galactic extinction along the line of sight at ZTF J0139+5245's coordinates is large, however (0.84, Schlafly & Finkbeiner 2011), and may be underestimated at its relatively nearby distance ($d = 172.9 \pm 7.4$ pc, Bailer-Jones et al. 2018) due to locally dense regions within the ISM. The additional extinction may also be caused by the circumstellar material in this system.

3.2. Calcium Absorption

In the combined spectrum for each night we detect a Ca II K absorption feature (3934 Å), and on some nights a Ca II H absorption feature as well (3968 Å, Figure 3). Three possible origins can explain the detected Ca absorption: (1) gas in the interstellar medium, (2) Ca in the photosphere of the white dwarf, or (3) circumstellar metallic gas. All three may contribute to some degree.

To explore the relative importance of each possibility, we first assess the Ca II K line strength for each night by assuming a purely photospheric origin and modeling the line using the atmosphere code of Koester (2010). On nights one through three, outside of a deep transit but just a few days after the nearest transit event, we find [Ca/H] abundances of -5.5 ± 0.3, -5.3 ± 0.3, and -4.9 ± 0.3, respectively. The uncertainties were empirically determined assuming that these first three nights are random samplings of a constant photospheric Ca abundance. On night four, at roughly 15% transit depth, we find [Ca/H] $= -4.6 \pm 0.3$ (Figure 3). While only 2σ higher relative to the lowest measured abundance, the variable line strength rules against a predominantly interstellar origin.

If the observed Ca absorption is purely photospheric, these abundances would be at the upper end of Ca pollution detected in DA white dwarfs of similar temperatures (see Figure 1 in Koester & Wilken 2006), and would indicate a high rate of metal accretion onto the white dwarf whose Ca diffusion timescale is 1–10 years (Koester & Wilken 2006; Cunningham et al. 2019). There may also be contributions from circumstellar metallic gas along the line of sight, however, in which case the

derived [Ca/H] values should be considered overestimates of the photospheric calcium abundance.

Absorption features with both photospheric and circumstellar components would likely exhibit two features at different velocities due to the gravitational redshift at the white dwarf surface. This difference would be $\approx$24 km s^{-1} for a 0.52 $M_{\odot}$ white dwarf, which corresponds to a wavelength difference of 0.3 Å for Ca II K. With a resolution of 1.9 Å, our spectra would be unable to resolve these components. While unresolved, if the increase in Ca absorption is due primarily to circumstellar gas with a fixed photospheric component, a small shift in the velocity of the blended line is expected. Unfortunately, we find that the velocity uncertainties for our spectra are of order 50 km s^{-1} on most nights, preventing any meaningful comparison between nightly line velocities.

We note, however, that during the observations in transit on night four, the Ca II K line cannot be fit adequately with a purely photospheric model. For the large Ca abundance required to match the strength of the observed line, intrinsic broadening exceeds the spectral resolution of our data, whereas the observed Ca II K line remains unresolved (Figure 3). This suggests that the increased Ca II absorption on night four is caused partly by an increased column density of metallic gas along the line of sight. With only one night of in-transit spectroscopy, however, the exact relationship between transit events and Ca II absorption in ZTF J0139+5245 remains unclear. Spectroscopic observations at higher resolution across the full orbital period are needed to assess the presence of both photospheric and circumstellar components and understand their relationship with the transiting material.

3.3. ZZ Ceti Pulsations

The 3D spectroscopic $T_{\rm eff}$ and $\log(g)$ place ZTF J0139+5245 inside the ZZ Ceti instability strip (Gianninas et al. 2015), where H-atmosphere white dwarfs pulsate. To assess whether any significant variability exists at periods expected of ZZ Cetis, we analyze the nine nights of McDonald 2.1 m high-speed photometry taken out of transit. For the Lomb–Scargle periodogram of the combined McDonald light curve, we estimate a 0.1% false alarm probability threshold of 0.37% using four times the average amplitude of the periodogram, $4\langle A\rangle$, between 500 and 10,000 μHz (Breger et al. 1993; Kuschnig et al. 1997). We find two significant peaks that rise above this threshold at 968 μHz and 1113 μHz (see Figure 4).

Owing to strong aliasing caused by large gaps in the data, we assume an extrinsic error for our frequencies equal to the daily alias (11.6 μHz), which matches the spacing between large adjacent peaks in the spectral window. The two significant peaks have periods of 1030 and 900 s, respectively, consistent with red-edge ZZ Cetis (Mukadam et al. 2006). The pulsational variability can also be seen by eye in the McDonald photometry, most notably in the sixth and seventh panels of Figure 4. The lack of visible variations on some nights is typically inferred as the destructive beating between independent modes, a common characteristic of multiperiodic ZZ Cetis, but may also be due to increased statistical noise on nights with relatively poor weather.

The presence of pulsations in ZTF J0139+5245 pose an additional challenge for measuring Ca line strength variations since the effective temperature of a white dwarf can change by hundreds to thousands of degrees throughout a pulsation cycle. We expect this effect to be relatively small in our analysis because the combined spectra for each night are averaged over several pulsation cycles, and the pulsation amplitudes observed appear small on average relative to other ZZ Cetis. G29-38, for instance, is both a metal polluted and high amplitude ZZ Ceti whose Ca II K equivalent width varies by <10% throughout a typical pulsation cycle (von Hippel & Thompson 2007; Debes & López-Morales 2008; Thompson et al. 2010). When averaged over many pulsation cycles, the equivalent width variations due to pulsations in G29-38 are expected to drop well below the 5% level even in the worst case scenario with its highest amplitude pulsations (von Hippel & Thompson 2007). In our case, even a 5% effect would be small relative to the measurement uncertainties, but future studies of ZTF,J0139+5245 at high resolution and high signal-to-noise might need to take this effect into account.

3.4. The Transit Spacing

In total, we detect two full transit events in the public ZTF data and a third full transit in our LCOGT follow-up observations. A transit egress is also seen at the start of LCOGT observations, around MJD = 58655. We constrain the transit spacing by phase-folding all of these data to obtain a close match between the observed transit start times. This occurs with a folding period of 107.2 days (see Figure 5). Due to the consistent spacing observed between multiple transits, we infer this to be the orbital period of the transiting material.

After phase folding, we note that a few ZTF data points indicating a significant drop in flux lie near an expected transit event around 2019 February 25 (see Figure 5). The coverage is very sparse, however, and without a clear indication of transit ingress or egress, we cannot conclude whether these points represent a transit detection. In addition, we searched for transits among the 52 good-quality PS1 data points to further constrain the transit spacing, but find no indication of a transit detection distinguishable from statistical noise ($\Delta m > 0.15$ mag). Also, when folded at the 107.2 day period, no PS1 data points overlap with the deepest portions of the ZTF and LCOGT transits.

The three full transits observed are variable in both depth and duration. The first transit is the deepest ($\approx$40%) and longest ($\approx$25 days), while the third transit appears the shallowest ($\approx$20%) and shortest ($\approx$15 days). The second transit is <25 days long and sparsely sampled, but does appear to reach its lowest point much later relative to the first and third transits. Such behavior is reminiscent of WD 1145+017, whose debris-induced transits exhibit both orbit-to-orbit ($4.5 < P_{\rm orb} < 4.9$ hr) and years-long dynamical evolution of their depths, durations, and shapes (Vanderburg et al. 2015; Gänsicke et al. 2016; Redfield et al. 2017; Rappaport et al. 2018). KIC 8463852, an F-type main-sequence star with dust-induced transits, also shows irregularly shaped transits, although it has yet to exhibit conclusively periodic behavior over several years of observations (Boyajian et al. 2016; Schaefer et al. 2018). A variety of other objects are known with irregularly shaped transits (see, e.g., Rappaport et al. 2019), and are mostly attributed to dusty occulting material.

4. Discussion

4.1. A Potential Orbital Configuration

To account for the presence of transits in ZTF J0139+5245, we consider one possible model where a small rocky object

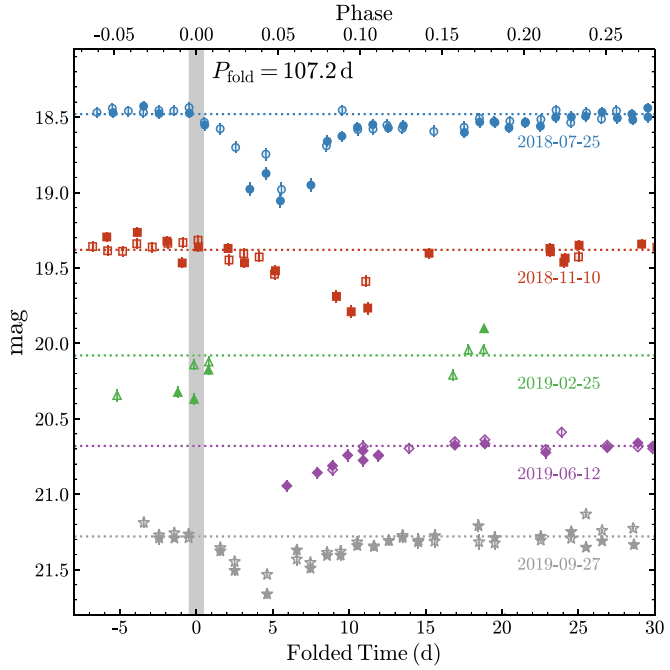

Figure 5. ZTF and LCOGT photometry folded on a period of 107.2 days and vertically shifted so each transit is visible. Shaded symbols denote ZTF-*r* and LCOGT-*rp* band data while open symbols denote ZTF-*g* and LCOGT-*gp* band data. The vertical gray line at phase = 0, with corresponding dates shown, denotes the epoch at which transits are expected to begin based on the 107.2 day period. The observed start of each transit is consistent with the folding period, but transit depths, durations, and shapes appear to vary (see Section 3.4). The ZTF data points around 2019 February 25 coincide with a predicted transit event, but are too sparsely sampled for conclusive evidence of a transit detection.

was at some point perturbed off its original orbit and brought close enough to the white dwarf to be tidally disrupted into a stream of dust and debris (Debes & Sigurdsson 2002; Jura 2003). Taking the observed ZTF transit spacing of 107.2 days as the orbital period of that debris, which gives a semimajor axis of $a = 76.4\,R_\odot$ (0.355 au), and assuming the material is currently orbiting near to or within the Roche limit ($r_{\rm R}$, Roche 1849) at periastron, a high eccentricity is required. Adopting for the disrupted body the average density of asteroids ($\rho \approx 3.0\,{\rm g\,cm^{-3}}$; Carry 2012), we find $r_{\rm R}$ for ZTF J0139+5245 to be $1.5\,R_\odot$ (Rappaport et al. 2013). Using $r_{\rm R}$ as the orbiting material's periastron distance implies an eccentricity of $e > 0.97$ and an apastron distance of $\approx 150\,R_\odot$ (0.70 au).

At periastron, a single dust grain would take <1 minute to transit the white dwarf, and at apastron ≈1.5 hr. Much longer transits are observed by ZTF, suggesting the presence of an extended stream of debris. Large planetesimals may be embedded within this material, but our current constraints on short-timescale transit events from ZTF and McDonald are weak due to sparse coverage.

We estimate a lower limit on the mass of the transiting material that passes between the white dwarf and Earth by first calculating the equivalent width for one of the ZTF transits. The total amount of white dwarf light blocked during the first ZTF transit is equivalent to a total eclipse lasting four days. Since we have no constraints on the density or radial extent of the transiting material, we model this equivalent total eclipse using a flat rectangular cloud composed of nonoverlapping, opaque spherical particles. The cloud has a height equal to the white dwarf diameter and a width equal to the equivalent transit duration multiplied by the Keplerian velocity of the orbiting material. If transiting at an orbital distance of 1.5 $R_\odot$, the required mass of the occulting material is

$$M_d \approx 7 \times 10^{18} \left[\frac{r_d}{1\ \mu{\rm m}}\right]\left[\frac{\rho_d}{2\ {\rm g\ cm^{-3}}}\right] {\rm g}, \quad (1)$$

where r_d and ρ_d are the radius and density of a single spherical particle. If transiting at $150\,R_\odot$ (0.70 au), the mass estimate decreases to

$$M_d \approx 7 \times 10^{16} \left[\frac{r_d}{1\ \mu{\rm m}}\right]\left[\frac{\rho_d}{2\ {\rm g\ cm^{-3}}}\right] {\rm g}. \quad (2)$$

In both cases these masses are consistent with asteroid-sized objects, but represent only the observed transiting material. Also, relaxing the various assumptions we made would tend to increase the estimated mass. For instance, our assumption of nonoverlapping particles works well in the optically thin limit, but for the first ZTF transit we estimate a roughly 15% increase in mass when allowing for overlapping particles. We consider this a small effect, however, compared to the two orders-of-magnitude difference seen when choosing different orbital distances during transit. Our estimate also neglects mass contributed by gas in the system.

4.2. Possible Origins of the Transiting Material

The origin of the transiting material in ZTF J0139+5245 faces many of the same questions that have been posed for metal-polluted white dwarfs in general. During the post-main-sequence lifetime of the progenitor star, any planetary objects inside of at least 1.5 au are likely to be engulfed and destroyed (Mustill & Villaver 2012), and only objects with as much mass as a brown dwarf are expected to survive engulfment (Livio & Soker 1984; Soker et al. 1984; Nelemans & Tauris 1998; Maxted et al. 2006). To account for the prevalence of metal polluted white dwarfs, a mechanism is needed that can bring rocky planetary material to the surface of the white dwarf from outside the engulfment region. The canonical tidal disruption model provides such a mechanism, whereby asteroids are gravitationally perturbed to highly eccentric, star-grazing orbits following the orbital expansion of outer planets due to stellar mass loss (Debes & Sigurdsson 2002; Jura 2003). Subsequent works have shown that secular perturbations on asteroids work on timescales that match the observed age distribution of metal polluted white dwarfs (Frewen & Hansen 2014; Mustill et al. 2018; Smallwood et al. 2018).

The orbital period of the transiting material in ZTF J0139+5245 clearly places it within the region previously engulfed during post-main-sequence evolution, so again a mechanism is required that places material at this location. With irregularly shaped transits and Ca II K and H absorption lines of photospheric or circumstellar origin, the current observations are consistent with the standard tidal disruption model. However, given the long orbital period of the transiting material, this model requires a very high eccentricity to bring the material near to or within the Roche limit (see Section 4.1).

Such high eccentricities are expected during the initial infall and disruption event (Debes et al. 2012; Veras et al. 2014), but confirming a highly eccentric orbit is not possible with the observations presented here. Thus, the standard tidal disruption model remains just one possibility for the origin of the

observed transiting material. If confirmed, however, this model would provide a natural explanation for the potential variability observed in Ca II line strengths. Each pass at periastron may result in a gas production event due to sublimation or collisions so that the transiting material remains supplied with metallic gas. This way, an increased column density of metallic gas can be observed during transit, potentially accompanied by increased photospheric accretion.

Another possibility is that the transiting material is somehow related to an object that survived post-main-sequence engulfment. While objects less massive than brown dwarfs are typically expected to be destroyed, the recent detection of a giant planet in close orbit around WD J091405.30+191412.25 has shown that massive planets down to roughly $1\,M_J$ may survive engulfment as well (Gänsicke et al. 2019). Using the measured J-band magnitude from UKIRT (Dye et al. 2018), we can place limits on the presence of a companion. We find that $J = 19.10 \pm 0.07$ (AB mag) is consistent with the synthetic J-band magnitude (Holberg & Bergeron 2006) of an isolated white dwarf (see Figure 2). Using the absolute J-band magnitudes for L-dwarfs from Dupuy & Liu (2012), we can exclude the presence of any companion with a spectral type earlier than L6.

The orbital periods of post-common-envelope binaries with such low-mass companions are typically in the range of 0.1–1.0 days (Nebot Gómez-Morán et al. 2011; Camacho et al. 2014; Zorotovic et al. 2014) and, as shown in Section 4.1, the observed transit durations cannot be accounted for by a single solid object. In addition, the vast majority of metal-polluted white dwarfs with a detected infrared excess are single stars (Wilson et al. 2019). With these constraints, we find a brown dwarf or planetary mass companion that has survived common envelope evolution to be an unlikely source for the observed transits.

Radial velocity measurements throughout the orbit would place additional constraints on any companion mass, though even at the upper end of brown dwarf masses ($0.08\,M_\odot$), radial velocity semiamplitudes of just $\sim$5 km s^{-1} would be expected for an edge-on, circular orbit at the observed orbital period. The uncertainties in our current spectroscopic observations are too large to further rule out the presence of a companion.

Another mechanism that may transport planetary objects into the previously cleared-out region is the late unpacking of densely spaced planetary systems (Veras & Gänsicke 2015). Planet incursions alone cannot account for the 15–25 day transit durations observed, so a planet–planet or planet–asteroid collision must also occur to create an extended stream of planetary debris. The likelihoods of such collisions are poorly constrained, though Veras & Gänsicke (2015) state that 25% of terrestrial planet instabilities in their simulations are planet–planet collisions, and could be a plausible way to account for some heavily metal-polluted white dwarfs.

Lastly, regardless of how the observed planetary material was brought onto its current orbit around ZTF J0139+5245, there exist mechanisms beyond tidal disruption and collisions that may produce an extended stream of planetary debris. One possibility is the rotational fission of an aspherical asteroid (Makarov & Veras 2019; Veras et al. 2020). This mechanism does not require the asteroid to orbit within the Roche limit, though Veras et al. (2020) found that an asteroid around ZTF J0139+5245 must still achieve pericenter distances of 1–3 r_R for rotational breakup to occur, depending on how elongated the asteroid is.

5. Conclusions

We have presented the discovery of a white dwarf exhibiting photometric evidence for transits caused by planetary material orbiting far outside the Roche limit. We have placed loose constraints on the transit recurrence time ($\approx$107.2 days) and found transit-to-transit variations in depth (20%–45%), duration (15–25 days), and shape. We obtained the first optical spectra of ZTF J0139+5245 and identified the white dwarf as a DA due to strong Balmer lines, with $T_{\rm eff}^{\rm 3D} = 10,530 \pm 140$ K and $\log(g)^{\rm 3D} = 7.86 \pm 0.06$.

We detected Ca II H and K absorption features that are likely the result of photospheric metal accretion or an increase in circumstellar metallic gas along the line of sight. The strongest Ca lines were observed at 15%–20% transit depth, suggesting a correlation between transit events and increased calcium absorption. The change in Ca II K line strength is only 2σ significant in our data, however, so the variability of Ca absorption and its correlation with transit events needs verification with high-resolution spectroscopy over the entire orbital period. Additionally, James Webb Space Telescope (JWST) observations are needed for infrared flux constraints. Detection of an infrared excess could further rule out the possibility of a substellar companion, help measure the temperature of the circumstellar dust disk, and potentially reveal long-term infrared variability of the system.

While the observations presented here are consistent with the canonical tidal disruption model, the long orbital period requires a very high eccentricity ($e > 0.97$), which cannot yet be confirmed. Other mechanisms such as the rotational fission of aspherical asteroids (Makarov & Veras 2019; Veras et al. 2020), late planetary system unpacking (Veras & Gänsicke 2015), and collisions remain possible sources of the transiting debris, but we find an object that has survived post-main-sequence engulfment to be an unlikely source. If tidal disruption is indeed responsible for the observed transiting debris in ZTF J0139+5245, the long orbital period observed may suggest a much earlier phase of tidal disruption compared to WD 1145+017, whose transiting debris is also consistent with the tidal disruption model. Long-term monitoring of the transit periodicity may provide useful insight into the physical processes governing the evolution of its orbiting debris, such as Poynting–Robertson drag, collisions, and sublimation (Veras et al. 2015; Farihi 2016; Kenyon & Bromley 2017). Lastly, we expect a more systematic search of a larger space volume of white dwarfs in ZTF, and in future surveys such as the Large Synoptic Survey Telescope, will yield many more discoveries like ZTF J0139+5245.

The authors would like to thank J. Farihi for providing useful feedback on a draft of this article, D. Koester for the use of his models, and T. Marsh for developing and making available both PAMELA and MOLLY. Data from McDonald Observatory were obtained with financial support from NASA K2 Cycle 5 Grant 80NSSC18K0387 and the Wooten Center for Astrophysical Plasma Properties (WCAPP) under DOE grant DE-FOA-0001634. P.I. acknowledges financial support from the Spanish Ministry of Economy and Competitiveness (MINECO) under the 2015 Severo Ochoa Programme MINECO SEV20150548. B.T.G. was supported by the UK STFC grant

ST/P000495. This material is based upon work supported by the National Science Foundation under Award AST-1903828. The research leading to these results has received funding from the European Research Council under the European Unions Horizon 2020 research and innovation program No. 677706 (WD3D).

This work is based on observations obtained with the Samuel Oschin 48 inch Telescope at the Palomar Observatory as part of the Zwicky Transient Facility project, which is supported by NSF grant No. AST-1440341 and the participating institutions of the ZTF collaboration. We make use of observations and reduction software from the LCOGT network, and include data from the Pan-STARRS1 Surveys (PS1) and the PS1 public science archive, which have been made possible through contributions by participating institutions of the PS1 collaboration (https://panstarrs.stsci.edu/). This work makes use of the synthetic white dwarf colors provided by Pierre Bergeron (http://www.astro.umontreal.ca/~bergeron/CoolingModels).

We also make use of data from the United Kingdom Infra-Red Telescope from the year 2016 (UKIRT, http://www.ukirt.hawaii.edu/), the NASA Galaxy Evolution Explorer (GALEX, http://www.galex.caltech.edu/), the SDSS-III (http://www.sdss3.org/), and from the European Space Agency (ESA) mission Gaia (https://www.cosmos.esa.int/gaia) processed by the Gaia Data Processing and Analysis Consortium (DPAC, https://www.cosmos.esa.int/web/gaia/dpac/consortium).

Additional Software/Resources: Astropy (Astropy Collaboration et al. 2013, 2018), Photoutils (Bradley et al. 2019), IRAF (distributed by the National Optical Astronomy Observatory, which is operated by the Association of Universities for Research in Astronomy (AURA) under a cooperative agreement with the National Science Foundation.), the NASA Astrophysics Data System (ADS), and SIMBAD and VizieR (operated at CDS, Strasbourg, France).

ORCID iDs

Z. Vanderbosch https://orcid.org/0000-0002-0853-3464
E. Dennihy https://orcid.org/0000-0003-2852-268X
B. H. Dunlap https://orcid.org/0000-0002-1086-8685
P.-E. Tremblay https://orcid.org/0000-0001-9873-0121
B. T. Gänsicke https://orcid.org/0000-0002-2761-3005
K. J. Bell https://orcid.org/0000-0002-0656-032X
M. H. Montgomery https://orcid.org/0000-0002-6748-1748

References

Ahn, C. P., Alexandroff, R., Allende Prieto, C., et al. 2012, ApJS, 203, 21
Astropy Collaboration, Price-Whelan, A. M., Sipőcz, B. M., et al. 2018, AJ, 156, 123
Astropy Collaboration, Robitaille, T. P., Tollerud, E. J., et al. 2013, A&A, 558, A33
Bailer-Jones, C. A. L., Rybizki, J., Fouesneau, M., Mantelet, G., & Andrae, R. 2018, AJ, 156, 58
Bellm, E. C., Kulkarni, S. R., Graham, M. J., et al. 2019, PASP, 131, 018002
Boyajian, T. S., LaCourse, D. M., Rappaport, S. A., et al. 2016, MNRAS, 457, 3988
Bradley, L., Sipőcz, B., Robitaille, T., et al. 2019, astropy/photutils: v0.6, Zenodo, doi:10.5281/zenodo.2533376
Breger, M., Stich, J., Garrido, R., et al. 1993, A&A, 271, 482
Brown, T. M., Baliber, N., Bianco, F. B., et al. 2013, PASP, 125, 1031
Camacho, J., Torres, S., García-Berro, E., et al. 2014, A&A, 566, A86
Capitanio, L., Lallement, R., Vergely, J. L., Elyajouri, M., & Monreal-Ibero, A. 2017, A&A, 606, A65
Carry, B. 2012, P&SS, 73, 98
Chambers, K. C., Magnier, E. A., Metcalfe, N., et al. 2016, arXiv:1612.05560
Cunningham, T., Tremblay, P.-E., Freytag, B., Ludwig, H.-G., & Koester, D. 2019, MNRAS, 488, 2503
Debes, J. H., & López-Morales, M. 2008, ApJL, 677, L43
Debes, J. H., & Sigurdsson, S. 2002, ApJ, 572, 556
Debes, J. H., Walsh, K. J., & Stark, C. 2012, ApJ, 747, 148
Dupuy, T. J., & Liu, M. C. 2012, ApJS, 201, 19
Dye, S., Lawrence, A., Read, M. A., et al. 2018, MNRAS, 473, 5113
Evans, D. W., Riello, M., de Angeli, F., et al. 2018, A&A, 616, A4
Farihi, J. 2016, NewAR, 71, 9
Fitzpatrick, E. L. 1999, PASP, 111, 63
Fontaine, G., Brassard, P., & Bergeron, P. 2001, PASP, 113, 409
Frewen, S. F. N., & Hansen, B. M. S. 2014, MNRAS, 439, 2442
Fulton, B. J., Tonry, J. L., Flewelling, H., et al. 2014, ApJ, 796, 114
Gaia Collaboration, Brown, A. G. A., Vallenari, A., et al. 2018, A&A, 616, A1
Gänsicke, B. T., Aungwerojwit, A., Marsh, T. R., et al. 2016, ApJL, 818, L7
Gänsicke, B. T., Schreiber, M. R., Toloza, O., et al. 2019, Natur, 576, 61
Gentile Fusillo, N. P., Tremblay, P.-E., Gänsicke, B. T., et al. 2019, MNRAS, 482, 4570
Gianninas, A., Kilic, M., Brown, W. R., Canton, P., & Kenyon, S. J. 2015, ApJ, 812, 167
Girven, J., Gänsicke, B. T., Steeghs, D., & Koester, D. 2011, MNRAS, 417, 1210
Hewett, P. C., Warren, S. J., Leggett, S. K., & Hodgkin, S. T. 2006, MNRAS, 367, 454
Holberg, J. B., & Bergeron, P. 2006, AJ, 132, 1221
Horne, K. 1986, PASP, 98, 609
Indebetouw, R., Mathis, J. S., Babler, B. L., et al. 2005, ApJ, 619, 931
Jura, M. 2003, ApJ, 584, L91
Kaiser, N., Burgett, W., Chambers, K., et al. 2010, Proc. SPIE, 7733, 77330E
Kanaan, A., Kepler, S. O., & Winget, D. E. 2002, A&A, 389, 896
Kenyon, S. J., & Bromley, B. C. 2017, ApJ, 844, 116
Koester, D. 2010, MmSAI, 81, 921
Koester, D., Gänsicke, B. T., & Farihi, J. 2014, A&A, 566, A34
Koester, D., & Wilken, D. 2006, A&A, 453, 1051
Kuschnig, R., Weiss, W. W., Gruber, R., Bely, P. Y., & Jenkner, H. 1997, A&A, 328, 544
Liebert, J., Bergeron, P., & Holberg, J. B. 2005, ApJS, 156, 47
Lindegren, L., Hernández, J., Bombrun, A., et al. 2018, A&A, 616, A2
Livio, M., & Soker, N. 1984, MNRAS, 208, 763
Magnier, E. A., Schlafly, E., Finkbeiner, D., et al. 2013, ApJS, 205, 20
Makarov, V. V., & Veras, D. 2019, ApJ, 886, 127
Marsh, T. R. 1989, PASP, 101, 1032
Martin, D. C., Fanson, J., Schiminovich, D., et al. 2005, ApJL, 619, L1
Masci, F. J., Laher, R. R., Rusholme, B., et al. 2019, PASP, 131, 018003
Maxted, P. F. L., Napiwotzki, R., Dobbie, P. D., & Burleigh, M. R. 2006, Natur, 442, 543
Morrissey, P., Schiminovich, D., Barlow, T. A., et al. 2005, ApJL, 619, L7
Mukadam, A. S., Montgomery, M. H., Winget, D. E., Kepler, S. O., & Clemens, J. C. 2006, ApJ, 640, 956
Mustill, A. J., & Villaver, E. 2012, ApJ, 761, 121
Mustill, A. J., Villaver, E., Veras, D., Gänsicke, B. T., & Bonsor, A. 2018, MNRAS, 476, 3939
Nebot Gómez-Morán, A., Gänsicke, B. T., Schreiber, M. R., et al. 2011, A&A, 536, A43
Nelemans, G., & Tauris, T. M. 1998, A&A, 335, L85
Patterson, M. T., Bellm, E. C., Rusholme, B., et al. 2019, PASP, 131, 018001
Rappaport, S., Gary, B. L., Vanderburg, A., et al. 2018, MNRAS, 474, 933
Rappaport, S., Sanchis-Ojeda, R., Rogers, L. A., Levine, A., & Winn, J. N. 2013, ApJL, 773, L15
Rappaport, S., Zhou, G., Vanderburg, A., et al. 2019, MNRAS, 485, 2681
Redfield, S., Farihi, J., Cauley, P. W., et al. 2017, ApJ, 839, 42
Roche, E. 1849, Académie des Sciences de Montpellier: Mémoires de la Section des Sciences, 1, 243
Schaefer, B. E., Bentley, R. O., Boyajian, T. S., et al. 2018, MNRAS, 481, 2235
Schlafly, E. F., & Finkbeiner, D. P. 2011, ApJ, 737, 103
Smallwood, J. L., Martin, R. G., Livio, M., & Lubow, S. H. 2018, MNRAS, 480, 57
Soker, N., Livio, M., & Harpaz, A. 1984, MNRAS, 210, 189
Thompson, S., & Mullally, F. 2013, Wqed: Lightcurve Analysis Suite, Astrophysics Source Code Library, ascl:1304.004
Thompson, S. E., Montgomery, M. H., von Hippel, T., et al. 2010, ApJ, 714, 296
Tremblay, P. E., Bergeron, P., & Gianninas, A. 2011, ApJ, 730, 128
Tremblay, P. E., Ludwig, H. G., Steffen, M., & Freytag, B. 2013, A&A, 559, A104

Vanderburg, A., Johnson, J. A., Rappaport, S., et al. 2015, Natur, 526, 546
Veras, D. 2016, RSOS, 3, 150571
Veras, D., & Gänsicke, B. T. 2015, MNRAS, 447, 1049
Veras, D., Leinhardt, Z. M., Bonsor, A., & Gänsicke, B. T. 2014, MNRAS, 445, 2244
Veras, D., Leinhardt, Z. M., Eggl, S., & Gänsicke, B. T. 2015, MNRAS, 451, 3453
Veras, D., McDonald, C. H., & Makarov, V. V. 2020, MNRAS, 492, 5291
von Hippel, T., & Thompson, S. E. 2007, ApJ, 661, 477
Williams, K. A., Bolte, M., & Koester, D. 2009, ApJ, 693, 355
Wilson, T. G., Farihi, J., Gänsicke, B. T., & Swan, A. 2019, MNRAS, 487, 133
Zorotovic, M., Schreiber, M. R., & Parsons, S. G. 2014, A&A, 568, L9
Zuckerman, B., Melis, C., Klein, B., Koester, D., & Jura, M. 2010, ApJ, 722, 725